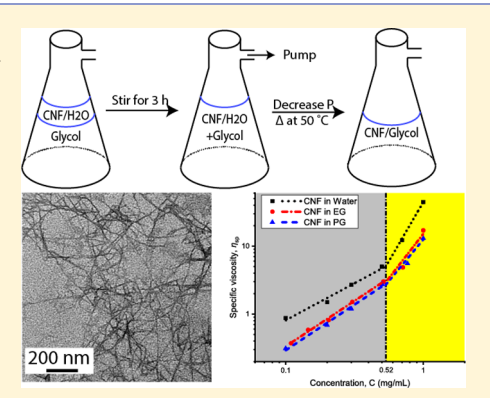
# 

# Morphology and Flow Behavior of Cellulose Nanofibers Dispersed in **Glycols**

Ruifu Wang,<sup>†</sup> Tomas Rosen,<sup>†</sup> Chengbo Zhan,<sup>†</sup> Shirish Chodankar,<sup>‡</sup> Jiahui Chen,<sup>§</sup> Priyanka R. Sharma,<sup>†</sup> Sunil K. Sharma, Tianbo Liu, and Benjamin S. Hsiao\*\*

Supporting Information

ABSTRACT: Understanding the morphology and flow behavior of cellulose nanofibers (CNFs) dispersed in organic solvents can improve the process of fabricating new cellulose-based nanocomposites. In this study, jute-based 2,2,6,6tetramethylpiperidinyl-1-oxyl (TEMPO)-oxidized CNFs with two different charge densities (0.64 and 1.03 mmol/g) were dispersed in ethylene glycol (EG) and propylene glycol (PG) using the solvent exchange method. The morphology and dimensions of CNFs in dry and suspension states were characterized using transmission electron microscopy, atomic force microscopy, and small-angle X-ray scattering techniques. The results showed that the crosssectional dimensions remained the same in different solvents. Rheological measurements revealed that CNF suspensions in water or glycol (EG and PG) behaved similar to typical polymer solutions with a solvent-independent overlap concentration corresponding to the crowding factor of about 14. Furthermore, a thixotropic behavior was found in the concentrated CNF/glycol systems as



observed in typical CNF aqueous suspensions. The fact that TEMPO-oxidized CNFs can be well dispersed in organic solvents opens up new possibilities to improve the CNF-polymer matrix blending, where the use of a viscous solvent can delay the transition to turbulence in processing and improve the control of fiber orientation because of a slower Brownian diffusive motion.

#### INTRODUCTION

Cellulose, as one of the most abundant natural polymers, has been thoroughly investigated in the past century in terms of morphology, 1-3 structural modifications, 4,5 and varying applications. 6,7 Recently, nanocellulose, having cross-sectional dimensions at the nanoscale, has attracted a great deal of attention because of its excellent mechanical property,8 stability, <sup>7,9,10</sup> biocompatibility, <sup>11</sup> functionalizability, <sup>12,13</sup> and diverse application potentials, including barrier films, <sup>14</sup> nanocomposite additives, <sup>15,16</sup> as well as water purification, <sup>17,18</sup> drug delivery, 19 and aerogel. 20 Typically, nanocellulose consists of two general types of subfamily: cellulose nanocrystal (CNC) and cellulose nanofiber (CNF, also denoted as nanofibrillated cellulose). A CNC is most commonly obtained through sulfuric acid hydrolysis, 1,21 whereas a CNF is usually obtained through oxidation or enzymatic treatment followed by highpressure mechanical homogenization.<sup>22</sup> Among the different methods to obtain CNFs, the 2,2,6,6-tetramethylpiperidinyl-1oxyl (TEMPO)-mediated oxidation process has proven to be a very effective pathway as the hydroxyl groups (-OH) at the C6 position of the cellulose chain can be regioselectively oxidized into carboxylate groups (-COO<sup>-</sup>), introducing electrostatic repulsion forces and thus improving the dispersibility of nanofibers in water.<sup>4</sup>

The physical properties of CNF are related to its structure and morphology, such as fiber dimensions (cross-sectional width and thickness, fiber length) and crystallinity. 13,23 As CNFs possess a very large aspect ratio, high flexibility, and abundant surface charges, the dispersed fibers can form a continuous network in the aqueous environment. 22,24 These unique properties make CNF a good reinforcing agent for fabricating strong nanocomposite materials, if the polymer matrix can also be dissolved in water. 16,25 The performance optimization of such cellulose-based nanocomposites requires a comprehensive understanding of the relationship among the structure, property, and processing (e.g., elongation and shear flows under steady-state and oscillating flow conditions). For the structural characterization of CNFs in suspensions, the small-angle X-ray scattering (SAXS) technique has been demonstrated as particularly effective to characterize the cross-sectional shape and dimensions as well as the aggregation

Received: May 20, 2019 Revised: June 24, 2019 Published: July 15, 2019

Department of Chemistry, Stony Brook University, Stony Brook, New York 11794-3400, United States

<sup>\*</sup>National Synchrotron Light Source II, Brookhaven National Laboratory, Upton, New York 11973-5000, United States

<sup>§</sup>Department of Polymer Science, The University of Akron, Akron, Ohio 44325-3101, United States

behavior in the suspension state. 26,27 Generally, the cross-sectional dimensions of CNFs in suspension determined by SAXS are quite consistent with those in the solid state determined by transmission electron microscopy (TEM, which can detect the fiber width) and atomic force microscopy (AFM, which is suitable for detecting the fiber thickness). 27,28 As the width of CNF (by TEM) is usually larger than the thickness (by AFM) of CNF, a ribbon-shaped cross-sectional model is particularly suited for the analysis of the SAXS data of TEMPO-oxidized CNF suspensions. 28

The flow properties of CNF suspensions are most commonly characterized by rheometry. <sup>24,29</sup> It is widely believed that the increasing number of homogenization steps during CNF preparation can increase the viscosity of TEMPO-oxidized CNFs<sup>30</sup> because of a higher level of defibrillation. In contrast, the increasing charge density often decreases the viscosity of the CNF suspension as the nanofiber network becomes more loosely connected. <sup>31</sup> There are several studies that reported that the CNF aqueous suspensions exhibited both multiregion shear-thinning behavior and linear shear-thinning behavior, <sup>32,33</sup> depending on the aspect ratio of CNFs extracted from different sources. In one study related to this work, Tanaka et al. demonstrated the relationship between the length distributions and the intrinsic viscosity for nanocellulose in water and glycerol mixtures. <sup>34</sup>

As a CNF can possess good suspension capability in water and also have excellent mechanical properties, it can be used as an effective filler or a percolation agent if the polymer matrix is hydrophilic. However, as most synthetic polymers are hydrophobic, the CNF suspension in different organic solvents has become an interesting subject for the possibility of creating new nanocomposite materials using different polymer matrixes. In this regard, Isogai et al.<sup>35</sup> have successfully dispersed TEMPO-mediated oxidized CNFs into varying organic solvents, such as dimethylsulfoxide (DMSO) and *N,N*-dimethylformamide (DMF) by the mixing and evaporation (water) routes. Furthermore, it has also been demonstrated that CNCs could be stably dispersed in DMF and DMSO through the freeze-drying and re-dispersing routes and could form a clear, stable, and thixotropic gel.<sup>36,37</sup>

Although CNFs are known to form stable suspensions in non-aqueous solvents, it remains unknown whether different solvents would affect their structure, morphology, suspension state, and the corresponding flow properties. In this study, two glycols, ethylene glycol (EG) and propylene glycol (PG), were selected because their general properties are similar to that of water but with a lower dielectric constant and higher viscosity. Application-wise, glycols are one of the reagents for making polyurethane, leading to the possibility of making CNF/ polyurethane nanocomposites.<sup>38</sup> In this study, combined SAXS and rheological measurements were carried out to carefully investigate the morphology and flow behavior of TEMPOoxidized CNFs dispersed in EG and PG, with variations of surface charge density on CNFs. Using the concept of crowding factor, the CNF network in the suspension was also described,<sup>24</sup> which was aimed to provide some new insights into the relationship among the morphology, aggregation, and flow behavior of CNFs dispersed in nonaqueous solvents.

# **■ EXPERIMENTAL SECTION**

Materials. Raw jute fibers were received from Toptrans Bangladesh Ltd.; TEMPO was purchased from Acros; sodium chlorite

(NaClO<sub>2</sub>, analytical standard) and sodium bromide (NaBr, analytical standard) were purchased from Sigma-Aldrich; sodium hypochlorite (NaClO, solution, 12.5 wt %) was obtained from Spectrum; sodium hydroxide (NaOH), 1,2-ethanediol (EG) were obtained from Fisher Scientific; and 1,2-propanediol (PG) was provided by VWR. All chemicals and samples were used without further purification. Deionized water (DI water) was used throughout the experiment.

**Preparation of CNFs.** The preparation of CNF samples from jute primarily followed the procedures developed by Saito and Isogai. 4 In brief, wet cellulose pulp (3 wt % of dry cellulose), after being bleached by NaClO2, was suspended in DI water at a concentration of 0.65 wt %. Subsequently, suitable amounts of NaBr (0.1 g/g dry cellulose) and TEMPO (0.01 g/g dry cellulose) were added to the slurry mixture. Two samples with different charge densities (or degree of oxidation), 0.64 mmol/g (hereafter referred to as "low charge") and 1.03 mmol/g (referred to as "high charge"), were obtained by using different amounts of oxidant NaClO (i.e., 11 mmol/g cellulose and 17 mmol/g cellulose of NaClO, respectively) added into the suspension dropwise under 500 rpm of stirring. The pH level of the suspension was maintained above 10 using 0.1 M NaOH (aq) during the reaction, which was stopped after 48 h by the addition of 10 mL of ethanol. The resulting cellulose slurry was dialyzed against DI water in a dialysis bag (Spectra/Por from Spectrum, MWCO: 6-8 kD) for 2 weeks until the conductivity of the water outside the dialysis bag was below 5  $\mu$ S.

The dialyzed slurry was diluted and passed through a high-pressure homogenizer (PandaPLUS, GEA Nitro Soavi) for six times under a pressure of 130–200 bar to obtain a homogeneous stock suspension. The resulting CNF suspension was centrifuged under a relative centrifugal force (rcf) of 4630 for 5 min to remove any large agglomerations. Finally, the CNF suspension was sonicated overnight prior to further characterization. The concentration of the suspension after homogenization was measured by the gravimetric analysis method.

Characterization of Charge Density. The charge density (carboxylate content) was obtained through a common conductometric titration method.<sup>4</sup> In this method, about 20 g of an aqueous CNF stock suspension was diluted to about 0.04 wt % and stirred for 3 h, where the pH level was adjusted to 3 by adding 0.01 mol/L of HCl solution. The CNF suspension was then titrated by a 0.05 mol/L of NaOH solution until the pH level reached 11. The conductivity of the suspension during titration was recorded by a conductivity meter (Oakton, CON 110 Series).

**Solvent Exchange.** The solvent exchange procedure was used to prepare CNF suspensions in EG and PG based on the method described by Dorris and Gray. The Depending on the desired concentration of the suspension, a proper amount of CNF aqueous suspension was mixed with 80 mL of EG or PG into a filtration flask (the density of the suspension was treated as the same as that of water), ensuring that the concentration of the stock suspension after the solvent exchange was 1.0 mg/mL. The mixture was continuously stirred at 300 rpm for approximately 1 h to achieve a homogeneous state. Water was subsequently removed by applying a vacuum pump under 50 °C for approximately 24 h (the evaporation of EG and PG was negligible), where the process was carefully monitored by weighing the suspension at certain time intervals.

The CNF/EG and CNF/PG samples were then prepared by diluting the stock suspensions into the desired concentrations, followed by vortex shaking and overnight sonication before further experiments. In this study, seven different CNF concentrations were prepared for each suspension system: 0.1, 0.15, 0.2, 0.3, 0.5, 0.7, and 1.0 mg/mL. The densities of all the suspensions were assumed to be the same as the solvent density during the dilution procedures, and the density of the dry CNF was estimated to be 1.5 g/cm<sup>3,39</sup> The solvent exchange process was repeated twice to keep the reproducibility of the samples. For comparison, CNF aqueous suspensions with different charge densities in desired concentrations were also prepared by directly diluting the CNF stock suspensions in water. The CNF suspensions dispersed in water, EG, and PG at a concentration of 1.0 mg/mL were centrifuged at 7500 rcf for 5 min

using a HERMLE Z-326 centrifuge to further verify the homogeneity of the suspensions.

Solution SAXS. Simultaneous SAXS and WAXS (wide-angle X-ray scattering) experiments of CNFs with different charge densities dispersed in EG and PG were conducted at the 16-ID beamline in National Synchrotron Light Source II (NSLS II), Brookhaven National Laboratory. The chosen X-rays had a wavelength  $(\lambda)$  of 0.79 Å, and the sample-detector distance was 3.6 m, which covered a  $q = (4\pi/\lambda) \sin(\theta)$ ,  $2\theta$  being the scattering angle) range of 0.005–2.0  $m \AA^{-1}$ . To reduce the sample degradation caused by X-ray radiation, a sample flow cell<sup>40</sup> was used. This flow cell consisted of a square channel of 1 mm opening, which was sandwiched between two Kapton films (DuPont 200HN) allowing the X-ray beam to pass through the channel. The suspension was circulated through the cell at a speed of 1 mL/h, which could avoid the radiation damage but without imposing shear-induced alignment. In the SAXS experiments, the concentration of the CNF/water, CNF/EG, or CNF/PG suspension was chosen at 1.0 mg/mL (CNFs at 1.03 mmol/g in EG at 0.7 mg/mL) to provide sufficient scattering contrast while minimizing the fiber-fiber interactions. For background subtraction, the scattering signals of pure water, EG, and PG were subsequently measured. Raw data processing, including the background subtraction, was performed by the MATLAB software. Prior to the subtraction, the background was first normalized with an experimental factor based on the main Kapton scattering peak at around 0.4  $\text{Å}^{-1}$ . The data analysis using the model fitting was carried out by the SASView software, developed by the Center for Neutron Research (NCNR) of the National Institute of Standards and Technology (NIST).

**Transmission Electron Microscopy.** The TEM sample preparation was as follows. Approximately 2.2  $\mu$ L of the diluted CNF suspension (below 0.1 mg/mL) was dropped on a carbon-coated copper grid, followed by staining using 2 wt % of uranyl acetate aqueous solution. The TEM measurements were performed using a JEOL JEM-1400 TEM instrument equipped with a Ruby camera, at the Center of Functional Nanomaterials in Brookhaven National Laboratory. The operating voltage of the instrument was set at 120 kV. The length and width estimations using TEM were based on more than 50 individual nanofibers measured in four different images.

Atomic Force Microscopy. In the AFM sample preparation, a drop of more diluted CNF suspension (0.01 mg/mL) was deposited onto a silica plate and dried (for CNF/EG and CNF/PG suspensions, gradual heating was used). The AFM measurements were performed using a Bruker Dimension ICON scanning probe microscope equipped with a 7 nm Broker OTE SpA tip in the tapping mode, at the Advanced Energy Research and Technology Center (AERTC), Stony Brook University.

**Ultraviolet–Visible (UV–Vis) Spectroscopy.** UV–vis spectroscopy of all CNF/water, CNF/EG, and CNF/PG suspensions at different concentrations and with different charge densities was performed with a Thermo Fisher GEN10S Spectrometer at room temperature. The chosen wavelength range was from 200 to 900 nm, where the spectrum was scanned at an interval of 1 nm. Pure EG and PG solvents were used as the background. The concentrations of the suspensions were corrected based on Beer's law.

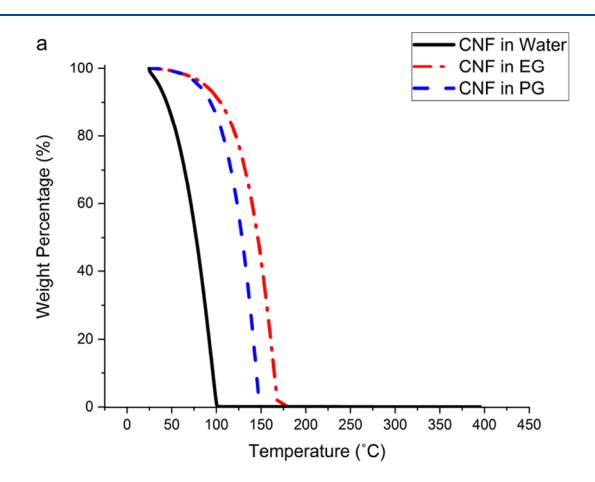
**Thermogravimetric Analysis.** TGA measurements were performed using a TA thermogravimetry instrument. The experiments were conducted on all the CNF/water, CNF/EG, and CNF/PG suspensions at the concentration of 1.0 mg/mL, ramping from room temperature to 400 °C at a rate of 10 °C/min under nitrogen protection.

Rheological Characterization. Rheological measurements were conducted using an Anton Paar Physica MCR-301 rheometer with the concentric cylinder geometry (the operation gap was 1.12 mm), where the viscosities of CNFs dispersed in water, EG, and PG at various concentrations and different charge densities were recorded. The zero-shear viscosity for each CNF suspension was estimated at the shear rate of 0.1 s<sup>-1</sup> and measured for 16 min based on the machine sensitivity. The experiments at steady shear were carried out in sequence from 1 to 1000 s<sup>-1</sup> with 10 different shear rates in each decade and 10 s at each shear rate. The CNF suspensions typically

exhibit a thixotropic behavior, that is, they exhibited a decrease of viscosity at a given shear rate with time. To study this phenomenon, another steady shear sequence from 1000 to 1 s $^{-1}$  was added to the original steady shear experiment. Preshearing, if required, was conducted at  $100 \, {\rm s}^{-1}$  for  $60 \, {\rm s}$  right before the shear loop experiment. Prior to the rheological measurements, all samples were equilibrated at 25 °C for 5 min to eliminate any internal stress during sample loading.

# ■ RESULTS AND DISCUSSION

Dimensions and Morphology of CNFs in Suspensions. All CNF/EG and CNF/PG suspensions (CNFs with both charge densities) at 1.0 mg/mL showed good homogeneity through visual inspection after centrifugation, where no precipitation or condensed flocculation was observed. The TGA results (Figure 1) indicated that both



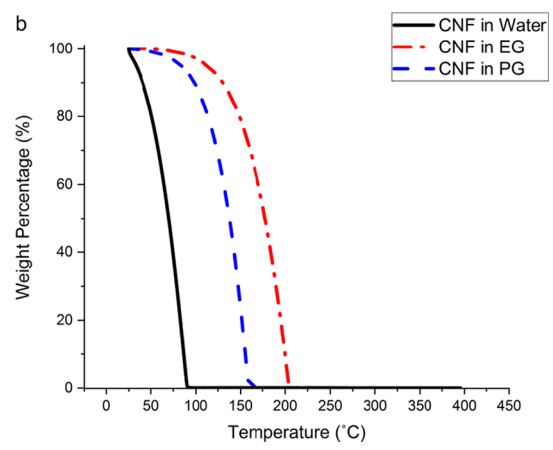


Figure 1. Normalized TGA curves for (a) CNFs of low charge (0.64 mmol/g) suspensions and (b) CNFs of high charge (1.03 mmol/g) suspensions.

CNF/glycol suspensions were free of unbound water, as no mass changes were observed at around  $100\,^{\circ}\text{C}$ . In TGA curves, we detected trace amounts of solids at high temperatures, and they were due to the salt used during the CNF fabrication process. The UV–vis spectra (Figure S1, Supporting Information) also confirmed that all samples exhibited good visible-light transmittance ( $400-700\,\text{nm}$ ), which was consistent with the observation that CNFs were well dispersed in both EG and PG solvents.

The investigation of the CNF morphology in suspensions with different solvents was carried out by the combined TEM,

AFM, and SAXS techniques, which complemented each other. Both TEM and AFM measurements provided real-space images of the system in the dry state, where local aggregates and fiber dimensions could be identified (fiber length and width were determined by TEM, and the fiber thickness was determined by AFM). However, the statistical significance of the quantification regarding the object dimensions in the TEM and AFM images often relies on sufficient sampling where many images need to be analyzed. In addition, there is some uncertainty related to the TEM width measurement as the boundary of the nanofibers cannot be precisely defined. Furthermore, the drying process during sample preparation may also introduce uncertainty with regard to the curvature or deposition of the CNF particles if they truly represent the dispersion state. For this reason, we also complemented the microscopic measurements with the SAXS study, which detects the mean fiber cross-sectional dimensions in suspension directly using an appropriate model based on microscopic observations.

The TEM images of CNFs prepared from the aqueous suspensions having CNFs of low charge (0.64 mmol/g) and high charge (1.03 mmol/g) are shown in Figure 2 (the TEM

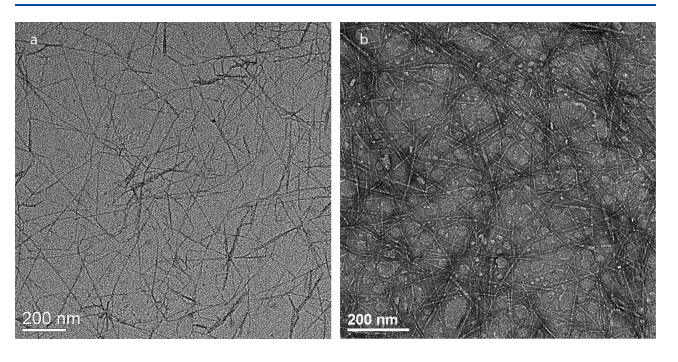


Figure 2. TEM images of (a) CNFs of low charge and (b) CNFs of high charge in water.

images of CNFs in EG and PG are shown in Figure S2, Supporting Information). In Figure 2, the average length and width were found to be 830.1  $\pm$  160.0 and 6.8  $\pm$  1.8 nm, respectively, for the CNFs of low charge, whereas they were  $881.0 \pm 163.6$  and  $5.8 \pm 0.9$  nm, respectively, for the CNFs of high charge. The TEM images showed that both straight and bent fibers were present, likely because of the combination of highly crystalline regions, dominating the straight regions, and the amorphous/paracrystalline regions, dominating the bend/ kink regions.41 The AFM images of the same aqueous suspensions are shown in Figure 3 (the AFM images of CNF/EG and CNF/PG suspensions are shown in Figure S3, Supporting Information). The average heights (or fiber thicknesses) were found to be 2.6  $\pm$  1.1 and 2.0  $\pm$  0.6 nm for the CNFs of low and high charges, respectively. In Figure 3, both isolated nanofibers and some aggregates were observed, where the aggregates were probably formed during sample preparation. However, we were unable to observe the twist or chiral structures that have been reported earlier, 42,43 probably because of the resolution limit of the instrument and the quality of the substrate. The TEM/AFM determination of the dimensions (length, width, and thickness) of CNFs prepared from different solvents are shown in Table S1. It was seen that these dimensions remained the same for the CNFs of same charge density regardless of the solvent used, as expected. The

increase in the charge density (or the degree of oxidation) notably decreased the averaged cross-sectional dimensions (width by about 13% and thickness by about 18%) but did not significantly change the fiber length.

SAXS measurements were conducted on CNF/water, CNF/EG, and CNF/PG suspensions. As the obtained SAXS profile is mainly because of the form factor of the nanofiber cross-sectional dimensions, some appropriate models are necessary to fit the scattering intensity I(q) data. The common models for CNFs are cylinder<sup>44</sup> and parallelepiped models.<sup>45</sup> The cylindrical model is clearly not consistent with the microscopic observation and is not considered. Recently, our group has demonstrated that a modified polydisperse ribbon model can provide a more accurate representation with regard to the shape of TEMPO-oxidized CNFs.<sup>28</sup> This model is expressed as

$$\frac{I(q)}{c} = \frac{2\pi}{q^3} \left\{ 1 - Re \left[ \left( 1 + \frac{iq\sigma_a^2}{a_0} \right)^{-(a_0/\sigma_a)^2} \right] \right\} (b_0^2 + \sigma_b^2) \\
\times {}_3F_2 \left( \frac{1}{2}, 1 + \frac{b_0^2}{2\sigma_b^2}, \frac{3}{2} + \frac{b_0^2}{\sigma_b^2}; \frac{3}{2}, 2; -\frac{q^2\sigma_b^4}{b_0^2} \right) \tag{1}$$

where I(q) is the scattering intensity, q is the scattering vector, c is the average fiber length, Re stands for the real part of the imaginary term inside the brackets, and  $_3F_2$  is a hypergeometric function that can be used to approximate the integration term at the original calculation of scattering intensity. The ribbon's cross section thus can be described by the parameters  $a_0$  and  $b_0$ , where  $a_0$  represents the height and  $a_0 + b_0$  is the width. The parameters  $\sigma_a$  and  $\sigma_b$  are the standard deviations of  $a_0$  and  $b_0$ , respectively. This model relies on the assumption that the fiber length c is much greater than the fiber height and width, which is fulfilled naturally for our samples.

The cross-sectional dimensions and the polydispersities of CNFs in suspensions of different solvents were obtained by fitting the SAXS profiles with a modified ribbon model. The obtained scattering data and the fitting curves for different CNF suspensions at the selected concentration (1.0 mg/mL for CNFs of both low and high charges, except for the CNFs of high charge in EG being at 0.7 mg/mL), are shown in Figure 4. Excellent agreement was obtained between the experimental data and the fitting curves (the R<sup>2</sup> coefficients were greater than 0.99 for all scattering profiles). The cross-sectional dimensions extracted from the fitted SAXS curves are shown in Table 1. It was seen that the fiber thickness  $(a_0)$  and width  $(a_0)$  $+ b_0$ ) determined by the SAXS analysis (Table 1) were slightly smaller than the values extracted from the AFM and TEM measurements (Table S1, Supporting Information). However, the SAXS results are probably closer to the statistically averaged dimensions of the dispersed CNFs. Nanofibers with very small dimensions are difficult to be accurately measured by the AFM/TEM image analysis, but the same fibers, even of a small fraction, can notably contribute to the scattering signal.

In Table 1, it was also found that the cross-sectional dimensions of CNFs remained almost the same when different solvents were used, similar to the AFM and TEM results (Table S1, Supporting Information). The average fiber thickness and width for CNFs of low charge were around 5.6 and 2 nm, respectively, whereas the average fiber thickness and width for CNFs of high charge were around 4.7 and 2 nm, respectively. The 2 nm fiber thickness is quite close to the

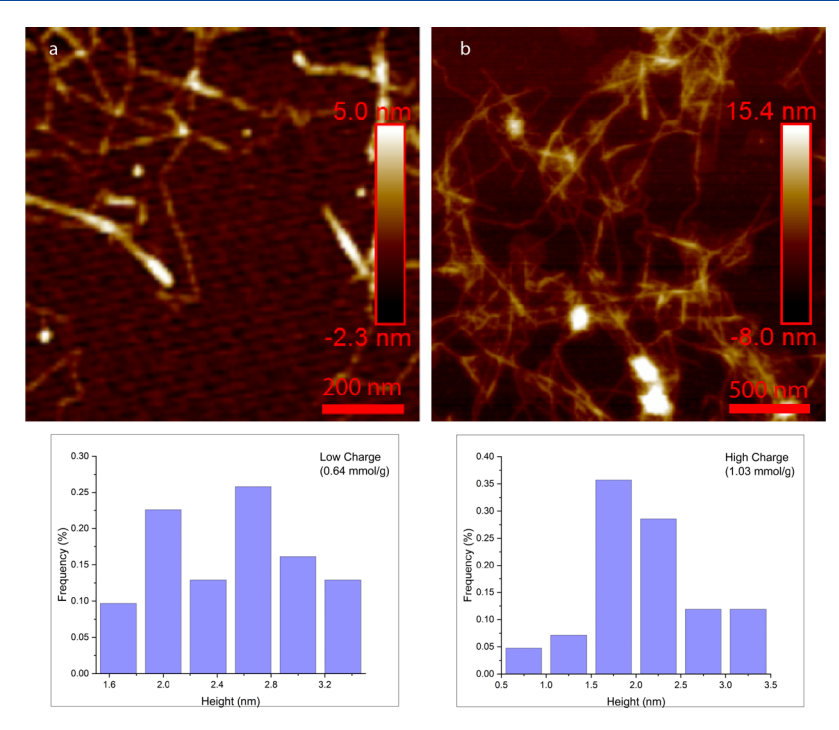


**Figure 3.** AFM images of CNFs prepared from aqueous suspensions and the corresponding thickness distributions for (a) CNFs of low charge and (b) CNFs of high charge.

value reported by Shimizu et al. 46 using AFM, whereas the 5.6 and 4.7 nm fiber widths are larger than the 3 nm reported by Fernandes et al.<sup>47</sup> using WAXS, which could be because of the different bioresources and pre- and post-treatments. These results indicated that CNFs with higher charge density possessed smaller cross-sectional dimensions, which could be attributed to a higher degree of defibrillation. This is consistent with the results from a previous study by Su et al., 48 where a thin fiber nanostrip with a monolayer thickness of 0.48 nm could be obtained under high TEMPO-mediated oxidation conditions. The resulting dimensions from the ribbon model were further compared with those obtained from a parallelepiped model, with the mean dimensions agreeing well regardless of the fitting model (Table S2, Supporting Information). We speculate that the ribbon is due to the lateral aggregation of elemental building blocks (probably containing 18 cellulose chains) in CNFs, whereas this topic will be further investigated by SAXS analysis and model simulation later.

Rheology of CNF/EG and CNF/PG Suspensions. Shear viscosity versus shear rate plots for CNF/EG and CNF/PG suspensions with CNFs of different charge densities and at varying concentrations are shown in Figure 5a—d. It was found that the rheological behavior of the CNF suspensions in glycols is very similar to that of a typical polymer solution, <sup>24,49</sup> that is, a pronounced shear-thinning behavior in concentrated CNF suspensions, where dilute suspensions behave like a Newtonian fluid. The same rheological features were also found in the corresponding aqueous systems (Figure S4, Supporting Information). As the viscosity order is PG > EG > water, the CNF/PG suspension also exhibited the highest viscosity (CNF/EG and CNF/PG suspensions in 1.0 mg/mL exhibited about 7 times and 15 times higher viscosity than that of the CNF/water suspension).

Generally, the viscosity—concentration relationship for a conventional polymer solution can be divided into three regimes based on the concept of overlap concentration  $(C^*)$ 

and entangled concentration  $(C_e)$ :<sup>49</sup> (1) dilute regime  $(C < C^*)$ , where polymer chains stay as a random coil with no interactions between the neighboring chains, (2) semidilute regime  $(C^* < C < C_e)$ , where the chains start interacting with each other but can still move freely, and (3) concentrated regime  $(C > C_e)$ , where the chains form a continuous network anchored by the chain entanglement. In the CNF/EG and CNF/PG suspensions, we were unable to determine the values of  $C_e$  because of the difficulty to prepare concentrated CNF/EG and CNF/PG suspensions (for the aqueous system, this could be achieved by evaporation of water). To determine  $C^*$ , specific viscosity  $(\eta_{\rm sp})$  was used, as this viscosity eliminates the role of the solvent impact. The value of  $\eta_{\rm sp}$  is defined as

$$\eta_{\rm sp} = \frac{\eta_0 - \eta_{\rm s}}{\eta_{\rm s}} \tag{2}$$

where  $\eta_0$  is the zero-shear viscosity and  $\eta_s$  is the viscosity of the solvent. In this study, the viscosity at a shear rate of 0.1 s<sup>-1</sup> was used as the zero-shear viscosity. The specific viscosity versus concentration plots for CNF/water, CNF/EG, and CNF/PG are shown in Figure 6. All figures clearly exhibited two linear relationships, with an intercept representing the overlap concentration. It was interesting to notice that the overlap concentration ( $C^* \approx 0.52 \text{ mg/mL}$  for CNFs of low charge;  $C^*$  $\approx$  0.33 mg/mL for CNFs of high charge) seemed to be solvent-independent, and they are in good agreement with a previous report.<sup>24</sup> For both CNFs of low and high charges, the  $\eta_{\rm sp}$  values of CNF/water were higher than those of CNF/EG and CNF/PG, which were about the same. In fact, for CNFs of the same charge, all three curves could be superimposed into one curve. The exponents describing the power law relationship between  $\eta_0$  and the concentration in the dilute and semidilute regimes are also shown in Figure 6a,b. In the dilute concentration regime, the exponent was found to be around 1 regardless of the surface charge on CNFs, whereas in the semidilute regime, the exponent was around 3. In terms of

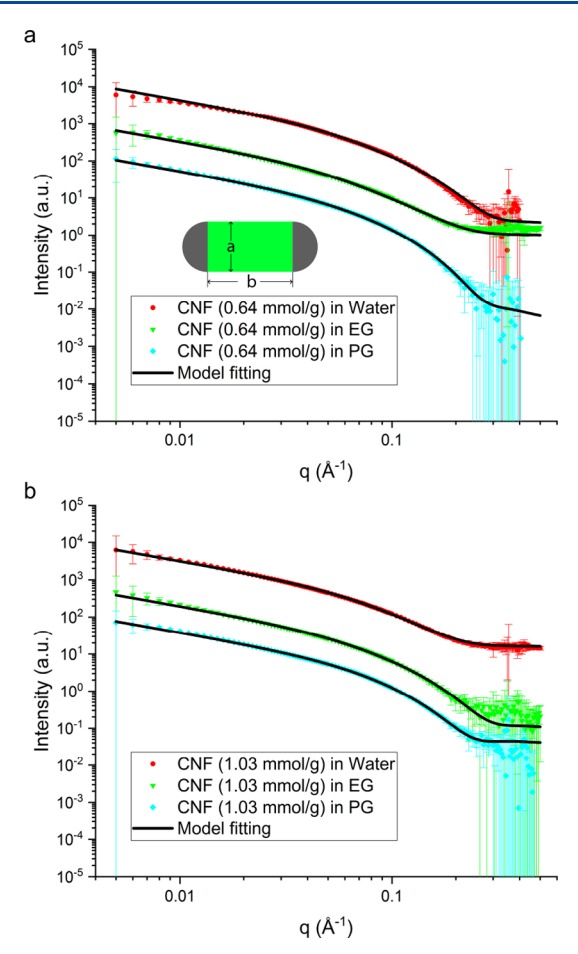


**Figure 4.** SAXS experimental data (after background subtraction) and fitting curves of (a) CNFs of low charge and (b) CNFs of high charge at 1.0 mg/mL (CNF of high charge in EG is 0.7 mg/mL). The intensity of the CNF/EG profile and that of the CNF/water profile were multiplied by a factor of 10 and 100, respectively, for visual comparison. A polydisperse ribbon model was used for the fit, and the extracted cross-sectional dimensions are shown in Table 1.

shear rheology, we thus can conclude that the CNF/EG and CNF/PG suspensions behave just like the aqueous system apart from the obvious difference in the solvent viscosity. This conclusion is consistent with the results from the earlier section, showing no change in the nanofiber morphology.

Crowding Factor and Overlap Concentration. The crowding factor (N) in a typical fiber suspension has been defined by Kerekes and Schell.<sup>50</sup> In short, N represents the number of fibers in a spherical volume, whose diameter equals the fiber length. The factor was derived based on the hypothesis that the entanglement contributes to the mechanical strength of the fiber network and is related to the

concentration of the suspension. The crowding factor thus can be described as

$$N = \frac{2}{3} \times \phi \times A^2 \tag{3}$$

where  $\phi$  is the volume fraction and A is the aspect ratio of the fiber (defined by the length of the fiber divided by the equivalent diameter). In this study, the value of A was calculated based on the assumption that the fiber has a circular cross section, the area of which is the same as that of the measured ribbon cross section.

Similar to the overlap concentration, it is thought that the viscosity of the fiber suspension can significantly increase when the volume fraction exceeds a critical value based on the concept of the crowding factor. This is because viscosity is a measure of momentum transfer within the fluid/suspension. As the momentum travels faster from fiber to fiber in a concentrated network, the transfer would require the presence of fiber—fiber contact points. As a result, the crowding factor, which can estimate the number of fiber—fiber contact points, becomes a major factor to determine the rheological property in the suspension of nanofibers. <sup>51</sup>

In CNF suspensions, the polydispersity of the fiber length should be taken into account when determining the crowding factor. Otherwise, the crowding factor would be underestimated as short fibers can also contribute to the number of contact points. To take this into account, Kropholler and Sampson<sup>52</sup> applied the following correction term to the crowding factor

$$N' = N(1 + CV^2)^4 (4)$$

where CV is the coefficient of variation (related to the polydispersity) and can be calculated by dividing the standard deviation of the length distribution with the value of the average length.

According to Kerekes et al., $^{50,51}$  the behavior of fiber suspensions can also be divided into dilute, semidilute, and concentrated regimes based on the N value. When N < 1, the suspension is in dilute regime and the fibers are free to move and rotate. On the other hand, when N > 60, corresponding to more than three contact points on each fiber, the suspension is in the concentrated regime and the fibers are locked into a network and lose their mobility. When the crowding factor is 1 < N < 60, there is no continuous network, but the fibers may locally flocculate in shear flow because of the shear-induced rotation. This is equivalent to the semidilute regime.

The aspect ratios for CNFs of low and high charges were calculated from the average cross-sectional dimensions (from SAXS) and the average fiber length (from TEM), and they were about 237 and 278, respectively. As the overlap concentration  $C^* = 0.52$  mg/mL,  $\phi = 0.035$  vol %, A = 237, and CV = 160/830 = 0.193 for CNFs of low charge and  $C^* = 0.035$  vol %.

Table 1. Cross-Sectional Dimensions of CNFs Dispersed in Different Solvents; These Dimensions Were Extracted from the Fitting of the SAXS Data Using a Modified Ribbon Model (Unit: nm)<sup>a</sup>

	PG			EG			water		
	$a_0$	$a_0 + b_0$	$\sigma_{a_0+b_0}$	$a_0$	$a_0 + b_0$	$\sigma_{a_0+b_0}$	$a_0$	$a_0 + b_0$	$\sigma_{a_0+b_0}$
CNFs (low charge)	2.1	5.4	2.2	1.6	6.1	2.3	1.7	5.4	2.2
CNFs (high charge)	2.0	4.5	1.9	1.8	4.7	2.0	1.7	5.0	1.8

 $a_0$ : fiber thickness;  $a_0 + b_0$ : fiber width;  $\sigma_{a_0+b_0}$ : the standard deviation of the fiber width.

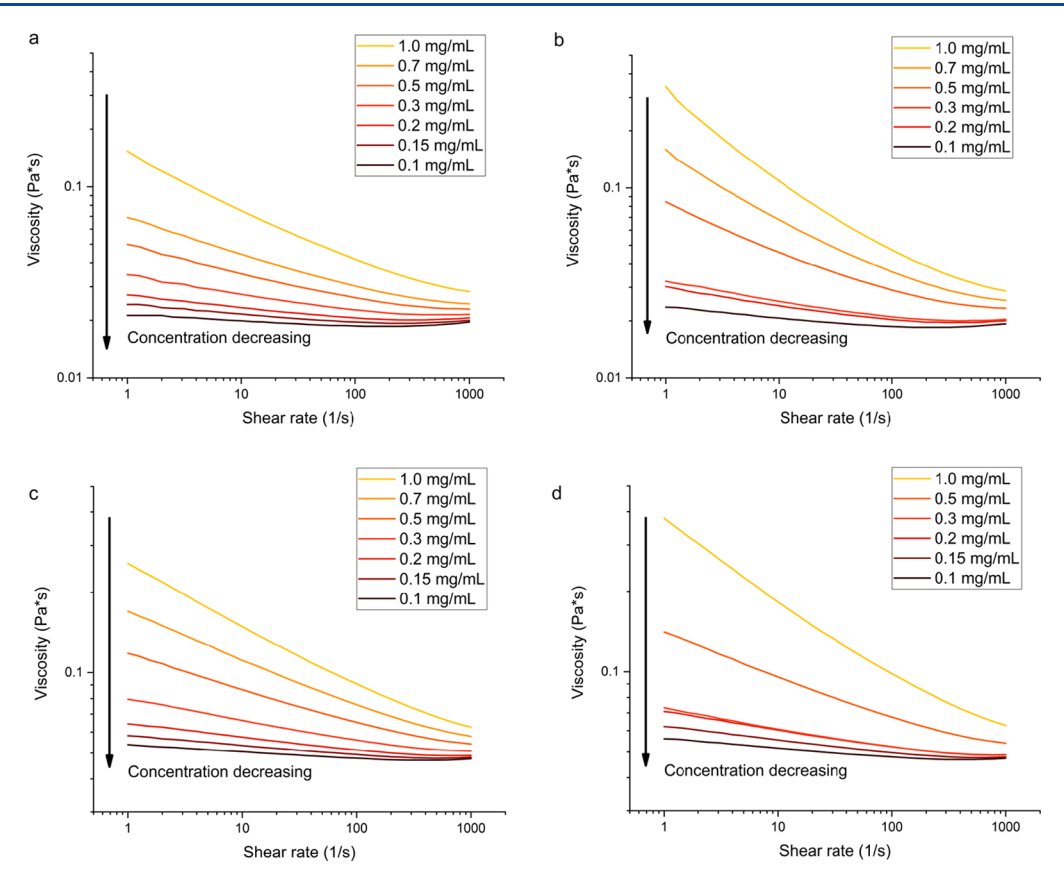


Figure 5. Shear-thinning behavior of CNF (low charge) suspensions in (a) EG and (c) PG and of CNFs (high charge) in (b) EG and (d) PG.

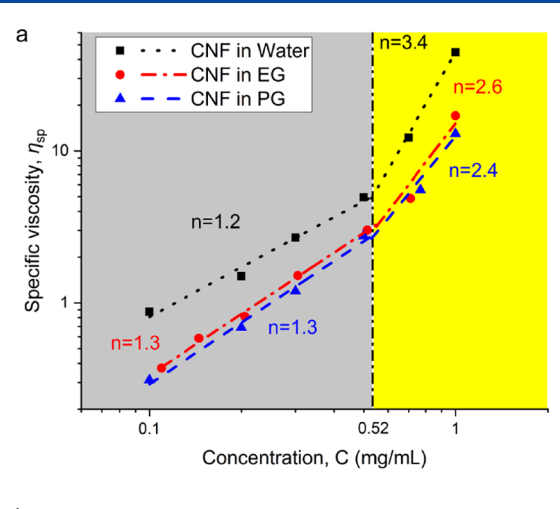
0.33 mg/mL,  $\phi$  = 0.023 vol %, A = 278, and CV = 164/881 = 0.186 for CNFs of high charge, we estimated the modified crowding factors N' of CNFs in suspensions at different charge densities and concentrations. These values are summarized in Table 2. It was found that the crowding factor N' ranged from 2 to 39 with a value close to 14 when the concentration was around  $C^*$ . This suggests that the dilute regime of all CNF suspensions is at N' < 14 and the transition to the semidilute regime occurs at N' > 14. Similar to the overlap concentration, which is solvent-independent, the crowding factor which dictates the regime change in a nanofiber suspension is also solvent-independent.

The crowding factor seems to be an essential parameter to correlate with the overlap concentration in the CNF suspensions. In this study, we found that at the overlap concentration,  $N' \approx 14$ , which is independent of the CNF charge density. This concept is useful to explain why the suspensions of CNFs with high charge generally exhibit higher viscosity values than those of CNFs with low charge, given the same volumetric concentration. However, these results are in contradiction to an earlier work, 31 which pointed out that the viscosity decreased with the increasing amount of carboxylate groups (and thus the surface charge). However, in these studies, it was also reported that the nanofiber length was strongly affected by the increased surface charge, where the aspect ratios of the fibers thus probably decreased accordingly.<sup>53</sup> In the present study, it was shown that the length of the CNFs remained about the same, but the cross-sectional dimensions decreased notably resulting in higher aspect ratios at a higher charge. This in turn led to a higher value of the crowding factor N' for CNFs of high charge than that for CNFs of low charge at the same concentration. The higher

crowding factor would result in a higher viscosity because of more fiber—fiber contact points. Another contributing factor, which is currently under investigation, is that more carboxylate groups on the fiber surface may also increase the friction between nanofibers, thus dissipating more energy and increasing the apparent viscosity.

As a final remark, although being sufficient to describe the CNF suspensions in the present study, the value of the crowding factor (N' = 14), where the overlap concentration was seen, is slightly different from our earlier studies reporting a value of N' = 16 for CNF suspensions.<sup>24</sup> There are several possible reasons for this discrepancy, including the use of different material sources for the CNF extraction, slight discrepancies in the pretreatment procedures resulting in different fiber dimensions, crystallinity, and fiber flexibility, the factors which all have impact on how the nanofibers behave in a shear flow. The fiber lengths could also have been slightly underestimated because of the measurement errors and/or insufficient statistics in the TEM image analysis.

Thixotropic Behavior. Another interesting rheological phenomenon reported for CNF suspensions is that they could exhibit a thixotropic behavior. The thixotropy of the samples in this study was investigated by measuring the viscosity continuously while increasing the shear rate, followed by the measurement upon decreasing the shear rate (more details in the Experimental Section), and the results are shown in Figure 7. The thixotropic behavior was observed in both CNF/EG and CNF/PG systems, as a higher viscosity value was found when the shear rate increased than that observed when the shear rate decreased. Generally, the thixotropic behavior of polymer solutions is because of the unequal rate of chain entanglement and disentanglement. The higher rate of chain



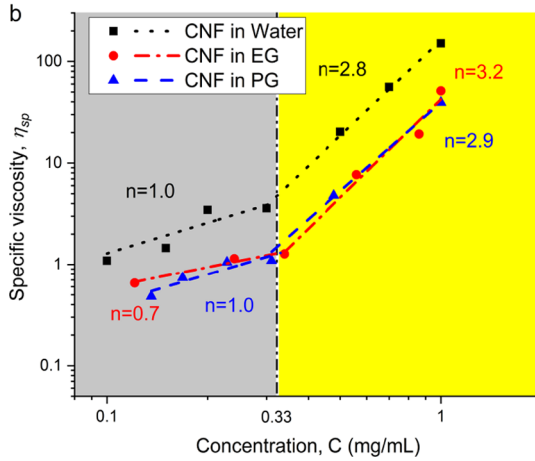


**Figure 6.** Specific viscosity of CNFs in different solvents as a function of concentration: (a) CNFs of low charge and (b) CNFs of high charge. "n" is the slope of the fitting curves.

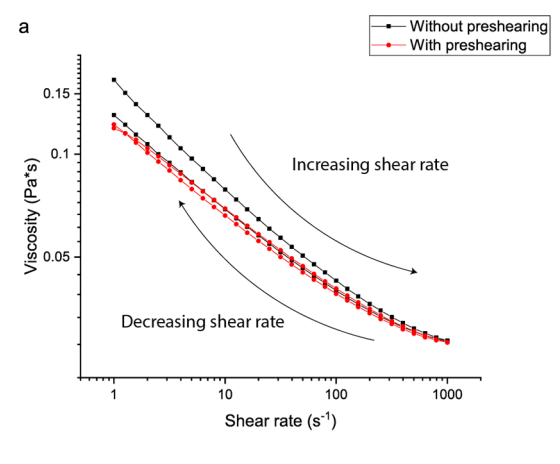
Table 2. Crowding Factors of CNFs in Different Concentrations and Charge Densities

		crowding factor $N'$							
concentration (mg/mL)	0.1	0.15	0.2	0.3	0.5	0.7	1.0		
low charge	2.9	4.3	5.8	8.7	15.0 <sup>a</sup>	20.2	28.9		
high charge	3.9	5.9	7.9	13.8 <sup>a</sup>	19.7	27.6	39.4		
<sup>a</sup> The crowding factor at the overlap concentration C*.									

disentanglement under shearing than re-entanglement can cause the higher viscosity while increasing the shear rate, which normally occurs in the concentrated regime  $C > C_{\rm e}$ . However, in this study, we find the thixotropic behavior even at lower concentrations, probably because of the local flocculation of CNFs. It is conceivable that when CNFs are stretched severely under strong shear, local flocs and agglomerations can be broken and disentangled, allowing the fibers to be aligned along the shear direction. To quantify the thixotropic behavior, a thixotropic index  $\alpha$ , defined by Benchabane and Bekkour, <sup>57</sup> is calculated according to

$$\alpha = 100 \times \frac{S_1 - S_2}{S_1} \% \tag{5}$$

where  $S_1$  and  $S_2$  are the areas under the curve of increasing viscosity and decreasing viscosity, respectively. The values of  $\alpha$ 



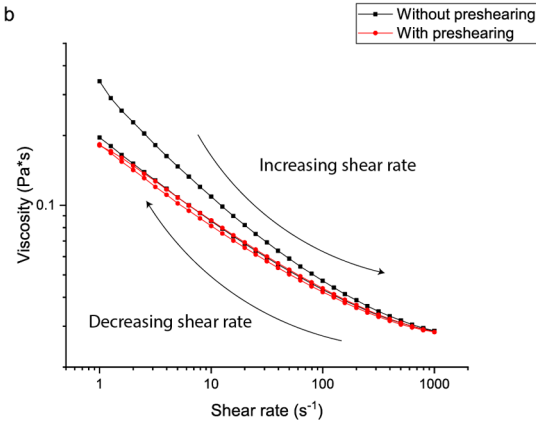


**Figure 7.** Thixotropic behavior of CNF/EG suspensions in 1.0 mg/mL for CNFs of (a) low charge and (b) high charge.

for the different CNF suspensions at 1.0 mg/mL are summarized in Table 3. From this table, it is evident that

Table 3. Thixotropic Indices of CNF Suspensions at 1.0  $\,\mathrm{mg/mL}$ 

	CNFs of low charge (%)		CNFs charg	of high ge (%)	dielectric constant		
PG	5.6	2.7 <sup>a</sup>	4.5	2.3 <sup>a</sup>	32		
EG	3.6	1.9 <sup>a</sup>	5.0	2.1 <sup>a</sup>	37		
water	0.5	$0.2^{a}$	1.5	$0.4^{a}$	79		
<sup>a</sup> The thixotropic index after preshearing.							

the thixotropic index is significantly higher for the glycol suspensions compared to the aqueous suspensions. This could be because of the slower Brownian rearrangement in the more viscous solvent in combination with less electrostatic repulsion forces, evident by the lower dielectric constants of glycols (Table 3). It is thought that the thermal motion and electrostatic repulsion of the fibers would facilitate the disentanglement of the nanofiber network during shearing, and therefore it might require higher shear rates to reach a state of more freely moving fibers. During the decreasing shear rate, Brownian motion is too weak for the re-entanglement of the disentangled fibers, resulting in a significantly lower viscosity. At rest, it would also take some time for the suspension to reach an entangled state because of the Brownian motion. This conclusion is further supported by the fact that the high thixotropic index of the glycol systems decreases to almost half of its original value after preshearing

(see Table 3 and Figure 7). It was found that the presheared CNF suspensions exhibited the near-identical viscosity and shear rate curves during both increasing and decreasing shear rate paths. This suggests that the presheared CNF suspensions were in a disentangled state, which is independent of the shear history.

The thixotropic indices of CNF/EG and CNF/PG dispersions in different concentrations are shown in Table S3 (Supporting Information). It was found that the values of  $\alpha$ were generally very low (<1%) for the dilute glycol suspensions  $(C < C^*)$ . In the concentration regime near and above the overlap concentration, the  $\alpha$  value generally was found to be larger for CNFs of low charge than that for CNFs of high charge (Table S3). This is because CNFs of low charge possess less electrostatic repulsion and would allow for a stronger network to form. However, this was not always the case (Table S3, the CNF/EG suspension at 1.0 mg/mL), and one also needed to consider the effect of the crowding factor. Generally, CNFs of high charge would possess a higher crowding factor than that of CNFs of low charge at the same concentration. Thus, the two effects (crowding factor and surface charge) are in competition to determine the thixotropic index. In the CNF/water and CNF/EG suspensions, the crowding factor is the dominant factor to determine the strength of the fiber network because the  $\alpha$  value is generally higher in the CNFs of high charge than that in the CNFs of low charge (Table 3). In CNF/PG suspensions, the electrostatic repulsion should be the dominant factor to affect the strength of the fiber network as  $\alpha$ is generally lower for CNFs of high charge. However the details of these effects are still under investigation.

# CONCLUSIONS

In this study, the morphology and rheology of CNF, dispersed in EG and PG, were studied in detail. Two CNF samples with the carboxylate content of 0.64 and 1.03 mmol/g, respectively, were used to investigate the effect of surface charge. It was found that the CNF morphology did not change with the use of different solvents, which led to the same overlap concentration. However, CNFs of high surface charge were found to possess smaller cross-sectional dimensions because of the higher degree of defibrillation. The rheological transition from the dilute to semidilute suspension could be described using the concept of crowding factor based on the fiber dimensions; the crowding factor for TEMPO-oxidized CNFs from jute at the overlap concentration  $(C^*)$  is around 14. The thixotropic behavior of the CNF suspensions was also studied. Both CNF/glycol suspensions showed a more pronounced thixotropic behavior compared to aqueous CNF suspensions. We believe that in CNF/glycol suspensions, the lower degree of Brownian motion because of higher solvent viscosity and the lower level of dissociation because of the carboxylated groups (lower dielectric constant) result in a more prominent thixotropic behavior, which occurred only at high concentrations (above C\*), as a strong fiber-fiber interaction is required for this phenomenon.

As a final remark, the fact that we can have stable suspensions of CNFs in glycol systems which behave just like the aqueous systems (although having much higher viscosity) has several promising future prospects. First, this opens up new opportunities for CNFs to be efficiently used in material composites with less hydrophilic synthetic polymers. Second, dispersing CNFs in a more viscous solvent also means that possibly certain processes can be improved as the flow of

the suspension can remain laminar at higher flow rates, owing to a lower Reynolds number compared to the equivalent aqueous system. A more viscous solvent can lead to slower Brownian diffusive dynamics and a lower rotary diffusion coefficient of the nanofibers. This would greatly improve the control of the fiber orientation through hydrodynamic forces.

## ASSOCIATED CONTENT

# **S** Supporting Information

The Supporting Information is available free of charge on the ACS Publications website at DOI: 10.1021/acs.macromol.9b01036.

UV-vis spectroscopy of CNFs of low (0.64 mmol/g) and high (1.03 mmol/g) charges in water, EG, and PG; TEM images of CNFs of low and high charges in EG and PG; AFM images of CNFs of low and high charges in EG and PG; plots of viscosity versus shear rate for CNFs of low charge and high charge dispersed in DI water; CNF dimensions in different solvents determined by TEM and AFM; and thixotropic indices of CNF/EG and CNF/PG dispersions in different concentrations (PDF)

#### AUTHOR INFORMATION

# **Corresponding Author**

\*E-mail: benjamin.hsiao@stonybrook.edu. Phone: +1(631) 632-7793.

# ORCID ®

Tomas Rosen: 0000-0002-2346-7063 Tianbo Liu: 0000-0002-8181-1790

Benjamin S. Hsiao: 0000-0002-3180-1826

# Notes

The authors declare no competing financial interest.

# ACKNOWLEDGMENTS

The authors would like to thank the financial support from the National Science Foundation (DMR-1808690). The authors would also like to thank Ms. Mengying Yang for assisting some rheological measurements, Dr. Chung-Chueh Chang at Advanced Energy Research & Technology Center (AERTC) for conducting AFM measurements, Dr. Lin Yang at the LiX beamline (16-ID) in NSLS II, BNL for assisting in SAXS experiments and data analysis. The LiX beamline is part of the Life Science Biomedical Technology Research resource, primarily supported by the National Institute of Health, National Institute of General Medical Sciences (NIGMS) under grant P41 GM111244, and by the DOE Office of Biological and Environmental Research under grant KP1605010, with additional support from NIH under grant S10 OD012331. As a National Synchrotron Light Source II facility resource at Brookhaven National Laboratory, work performed at the LSBR is supported in part by the U.S. Department of Energy, Office of Basic Energy Sciences Program under contract number DE-SC0012704. This research used resources of the Center for Functional Nanomaterials, which is a U.S. DOE Office of Science Facility, at Brookhaven National Laboratory under contract no. DE-SC12704.

# REFERENCES

- (1) Elazzouzi-Hafraoui, S.; Nishiyama, Y.; Putaux, J.-L.; Heux, L.; Dubreuil, F.; Rochas, C. The shape and size distribution of crystalline nanoparticles prepared by acid hydrolysis of native cellulose. *Biomacromolecules* **2008**, *9*, 57–65.
- (2) Saito, T.; Nishiyama, Y.; Putaux, J.-L.; Vignon, M.; Isogai, A. Homogeneous suspensions of individualized microfibrils from TEMPO-catalyzed oxidation of native cellulose. *Biomacromolecules* **2006**, *7*, 1687–1691.
- (3) Dufresne, A.; Cavaillé, J.-Y.; Vignon, M. R. Mechanical behavior of sheets prepared from sugar beet cellulose microfibrils. *J. Appl. Polym. Sci.* **1997**, *64*, 1185–1194.
- (4) Saito, T.; Isogai, A. TEMPO-mediated oxidation of native cellulose. The effect of oxidation conditions on chemical and crystal structures of the water-insoluble fractions. *Biomacromolecules* **2004**, *5*, 1983–1989.
- (5) Hubbe, M. A.; Rojas, O. J.; Lucia, L. A.; Sain, M. Cellulosic Nanocomposites: A Review. *BioResources* **2008**, *3*, 929–980.
- (6) Okaĥisa, Y.; Yoshida, A.; Miyaguchi, S.; Yano, H. Optically transparent wood-cellulose nanocomposite as a base substrate for flexible organic light-emitting diode displays. *Compos. Sci. Technol.* **2009**, *69*, 1958–1961.
- (7) Nogi, M.; Iwamoto, S.; Nakagaito, A. N.; Yano, H. Optically Transparent Nanofiber Paper. *Adv. Mater.* **2009**, *21*, 1595–1598.
- (8) Eichhorn, S. J.; Sirichaisit, J.; Young, R. J. Deformation mechanisms in cellulose fibres, paper and wood. *J. Mater. Sci.* **2001**, 36, 3129–3135.
- (9) Iwamoto, S.; Abe, K.; Yano, H. The effect of hemicelluloses on wood pulp nanofibrillation and nanofiber network characteristics. *Biomacromolecules* **2008**, *9*, 1022–1026.
- (10) Fukuzumi, H.; Saito, T.; Okita, Y.; Isogai, A. Thermal stabilization of TEMPO-oxidized cellulose. *Polym. Degrad. Stab.* **2010**, 95, 1502–1508.
- (11) Rodríguez, K.; Gatenholm, P.; Renneckar, S. Electrospinning cellulosic nanofibers for biomedical applications: structure and in vitro biocompatibility. *Cellulose* **2012**, *19*, 1583–1598.
- (12) Habibi, Y.; Lucia, L. A.; Rojas, O. J. Cellulose Nanocrystals: Chemistry, Self-Assembly, and Applications. *Chem. Rev.* **2010**, *110*, 3479–3500.
- (13) Moon, R. J.; Martini, A.; Nairn, J.; Simonsen, J.; Youngblood, J. Cellulose nanomaterials review: structure, properties and nanocomposites. *Chem. Soc. Rev.* **2011**, *40*, 3941–3994.
- (14) Fukuzumi, H.; Saito, T.; Iwata, T.; Kumamoto, Y.; Isogai, A. Transparent and High Gas Barrier Films of Cellulose Nanofibers Prepared by TEMPO-Mediated Oxidation. *Biomacromolecules* **2009**, *10*, 162–165.
- (15) Favier, V.; Chanzy, H.; Cavaille, J. Y. Polymer Nanocomposites Reinforced by Cellulose Whiskers. *Macromolecules* **1995**, 28, 6365–6367.
- (16) Shimazaki, Y.; Miyazaki, Y.; Takezawa, Y.; Nogi, M.; Abe, K.; Ifuku, S.; Yano, H. Excellent thermal conductivity of transparent cellulose nanofiber/epoxy resin nanocomposites. *Biomacromolecules* **2007**, *8*, 2976–2978.
- (17) Ma, H.; Burger, C.; Hsiao, B. S.; Chu, B. Ultra-fine cellulose nanofibers: new nano-scale materials for water purification. *J. Mater. Chem.* **2011**, *21*, 7507–7510.
- (18) Soyekwo, F.; Zhang, Q.; Gao, R.; Qu, Y.; Lin, C.; Huang, X.; Zhu, A.; Liu, Q. Cellulose nanofiber intermediary to fabricate highly-permeable ultrathin nanofiltration membranes for fast water purification. *J. Membr. Sci.* **2017**, *524*, 174–185.
- (19) Kolakovic, R.; Peltonen, L.; Laukkanen, A.; Hirvonen, J.; Laaksonen, T. Nanofibrillar cellulose films for controlled drug delivery. *Eur. J. Pharm. Biopharm.* **2012**, 82, 308–315.
- (20) Hayase, G.; Kanamori, K.; Abe, K.; Yano, H.; Maeno, A.; Kaji, H.; Nakanishi, K. Polymethylsilsesquioxane-Cellulose Nanofiber Biocomposite Aerogels with High Thermal Insulation, Bendability, and Superhydrophobicity. ACS Appl. Mater. Interfaces 2014, 6, 9466—9471.

(21) Bai, W.; Holbery, J.; Li, K. A technique for production of nanocrystalline cellulose with a narrow size distribution. *Cellulose* **2009**, *16*, 455–465.

- (22) Zimmermann, T.; Bordeanu, N.; Strub, E. Properties of nanofibrillated cellulose from different raw materials and its reinforcement potential. *Carbohydr. Polym.* **2010**, *79*, 1086–1093.
- (23) Saito, T.; Kimura, S.; Nishiyama, Y.; Isogai, A. Cellulose nanofibers prepared by TEMPO-mediated oxidation of native cellulose. *Biomacromolecules* **2007**, *8*, 2485–2491.
- (24) Geng, L.; Mittal, N.; Zhan, C.; Ansari, F.; Sharma, P. R.; Peng, X.; Hsiao, B. S.; Söderberg, L. D. Understanding the Mechanistic Behavior of Highly Charged Cellulose Nanofibers in Aqueous Systems. *Macromolecules* **2018**, *51*, 1498–1506.
- (25) Takagi, H.; Asano, A. Effects of processing conditions on flexural properties of cellulose nanofiber reinforced "green" composites. *Composites, Part A* **2008**, *39*, 685–689.
- (26) Geng, L.; Peng, X.; Zhan, C.; Naderi, A.; Sharma, P. R.; Mao, Y.; Hsiao, B. S. Structure characterization of cellulose nanofiber hydrogel as functions of concentration and ionic strength. *Cellulose* **2017**, *24*, 5417–5429.
- (27) Mao, Y.; Liu, K.; Zhan, C.; Geng, L.; Chu, B.; Hsiao, B. S. Characterization of Nanocellulose Using Small-Angle Neutron, X-ray, and Dynamic Light Scattering Techniques. *J. Phys. Chem. B* **2017**, 121, 1340–1351.
- (28) Su, Y.; Burger, C.; Hsiao, B. S.; Chu, B. Characterization of TEMPO-oxidized cellulose nanofibers in aqueous suspension by small-angle X-ray scattering. *J. Appl. Crystallogr.* **2014**, *47*, 788–798.
- (29) Nechyporchuk, O.; Belgacem, M. N.; Pignon, F. Current Progress in Rheology of Cellulose Nanofibril Suspensions. *Biomacromolecules* **2016**, *17*, 2311–2320.
- (30) Grüneberger, F.; Künniger, T.; Zimmermann, T.; Arnold, M. Rheology of nanofibrillated cellulose/acrylate systems for coating applications. *Cellulose* **2014**, *21*, 1313–1326.
- (31) Besbes, I.; Alila, S.; Boufi, S. Nanofibrillated cellulose from TEMPO-oxidized eucalyptus fibres: Effect of the carboxyl content. *Carbohydr. Polym.* **2011**, *84*, 975–983.
- (32) Nazari, B.; Kumar, V.; Bousfield, D. W.; Toivakka, M. Rheology of cellulose nanofibers suspensions: Boundary driven flow. *J. Rheol.* **2016**, *60*, 1151–1159.
- (33) Quennouz, N.; Hashmi, S. M.; Choi, H. S.; Kim, J. W.; Osuji, C. O. Rheology of cellulose nanofibrils in the presence of surfactants. *Soft Matter* **2016**, *12*, 157–164.
- (34) Tanaka, R.; Saito, T.; Hondo, H.; Isogai, A. Influence of Flexibility and Dimensions of Nanocelluloses on the Flow Properties of Their Aqueous Dispersions. *Biomacromolecules* **2015**, *16*, 2127–2131.
- (35) Okita, Y.; Fujisawa, S.; Saito, T.; Isogai, A. TEMPO-Oxidized Cellulose Nanofibrils Dispersed in Organic Solvents. *Biomacromolecules* **2011**, *12*, 518–522.
- (36) Dorris, A.; Gray, D. G. Gelation of cellulose nanocrystal suspensions in glycerol. *Cellulose* **2012**, *19*, 687–694.
- (37) Viet, D.; Beck-Candanedo, S.; Gray, D. G. Dispersion of cellulose nanocrystals in polar organic solvents. *Cellulose* **2007**, *14*, 109–113.
- (38) Lyman, D. J. Polyurethanes. I. The solution polymerization of diisocyanates with ethylene glycol. *J. Polym. Sci.* **1960**, *45*, 49–59.
- (39) Eichhorn, S. J.; Young, R. J.; Davies, G. R. Modeling crystal and molecular deformation in regenerated cellulose fibers. *Biomacromolecules* **2005**, *6*, 507–513.
- (40) Håkansson, K. M. O.; Fall, A. B.; Lundell, F.; Yu, S.; Krywka, C.; Roth, S. V.; Santoro, G.; Kvick, M.; Wittberg, L. P.; Wagberg, L.; Söderberg, L. D. Hydrodynamic alignment and assembly of nanofibrils resulting in strong cellulose filaments. *Nat. Commun.* **2014**, *5*, 4018–4027.
- (41) Puangsin, B.; Yang, Q.; Saito, T.; Isogai, A. Comparative characterization of TEMPO-oxidized cellulose nanofibril films prepared from non-wood resources. *Int. J. Biol. Macromol.* **2013**, *59*, 208–213.

(42) Arcari, M.; Zuccarella, E.; Axelrod, R.; Adamcik, J.; Sánchez-Ferrer, A.; Mezzenga, R.; Nyström, G. Nanostructural Properties and Twist Periodicity of Cellulose Nanofibrils with Variable Charge Density. *Biomacromolecules* **2019**, *20*, 1288–1296.

- (43) Usov, I.; Nystrom, G.; Adamcik, J.; Handschin, S.; Schutz, C.; Fall, A.; Bergstrom, L.; Mezzenga, R. Understanding nanocellulose chirality and structure-properties relationship at the single fibril level. *Nat. Commun.* **2015**, *6*, 7564.
- (44) Uhlig, M.; Fall, A.; Wellert, S.; Lehmann, M.; Prévost, S.; Wågberg, L.; von Klitzing, R.; Nyström, G. Two-Dimensional Aggregation and Semidilute Ordering in Cellulose Nanocrystals. *Langmuir* **2016**, 32, 442–450.
- (45) Cherhal, F.; Cousin, F.; Capron, I. Influence of Charge Density and Ionic Strength on the Aggregation Process of Cellulose Nanocrystals in Aqueous Suspension, as Revealed by Small-Angle Neutron Scattering. *Langmuir* 2015, 31, 5596–5602.
- (46) Shimizu, M.; Saito, T.; Nishiyama, Y.; Iwamoto, S.; Yano, H.; Isogai, A.; Endo, T. Fast and Robust Nanocellulose Width Estimation Using Turbidimetry. *Macromol. Rapid Commun.* **2016**, *37*, 1581–1586.
- (47) Fernandes, A. N.; Thomas, L. H.; Altaner, C. M.; Callow, P.; Forsyth, V. T.; Apperley, D. C.; Kennedy, C. J.; Jarvis, M. C. Nanostructure of cellulose microfibrils in spruce wood. *Proc. Natl. Acad. Sci. U.S.A.* **2011**, *108*, E1195–E1203.
- (48) Su, Y.; Burger, C.; Ma, H.; Chu, B.; Hsiao, B. S. Exploring the Nature of Cellulose Microfibrils. *Biomacromolecules* **2015**, *16*, 1201–1209.
- (49) McKee, M. G.; Hunley, M. T.; Layman, J. M.; Long, T. E. Solution rheological behavior and electrospinning of cationic polyelectrolytes. *Macromolecules* **2006**, *39*, 575–583.
- (50) Kerekes, R. J.; Schell, C. J. Characterization of Fiber Flocculation Regimes by a Crowding Factor. *J. Pulp Pap. Sci.* **1992**, *18*, J32–J38.
- (51) Celzard, A.; Fierro, V.; Kerekes, R. Flocculation of cellulose fibres: new comparison of crowding factor with percolation and effective-medium theories. *Cellulose* **2009**, *16*, 983–987.
- (52) Kropholler, H. W.; Sampson, W. W. The Effect of Fibre Length Distribution on Suspension Crowding. *J. Pulp Pap. Sci.* **2001**, *27*, 301–306.
- (53) Shinoda, R.; Saito, T.; Okita, Y.; Isogai, A. Relationship between Length and Degree of Polymerization of TEMPO-Oxidized Cellulose Nanofibrils. *Biomacromolecules* **2012**, *13*, 842–849.
- (54) Bettaieb, F.; Nechyporchuk, O.; Khiari, R.; Mhenni, M. F.; Dufresne, A.; Belgacem, M. N. Effect of the oxidation treatment on the production of cellulose nanofiber suspensions from Posidonia oceanica: The rheological aspect. *Carbohydr. Polym.* **2015**, *134*, 664–672.
- (55) Barnes, H. A. Thixotropy-a review. J. Non-Newtonian Fluid Mech. 1997, 70, 1-33.
- (56) Wang, L.; Gao, L.; Cheng, B.; Ji, X.; Song, J.; Lu, F. Rheological behaviors of cellulose in 1-ethyl-3-methylimidazolium chloride/dimethylsulfoxide. *Carbohydr. Polym.* **2014**, *110*, 292–297.
- (57) Benchabane, A.; Bekkour, K. Rheological properties of carboxymethyl cellulose (CMC) solutions. *Colloid Polym. Sci.* **2008**, 286, 1173–1180.